CHEMISTRY

Time-resolved dissolution elucidates the mechanism of zeolite MFI crystallization

Krassimir N. Bozhilov[1†], Thuy Thanh Le[2†], Zhengxing Qin[3], Tanguy Terlier[4], Ana Palčić[5], Jeffrey D. Rimer[2], Valentin Valtchev[6,7]*

Zeolite crystal growth mechanisms are not fully elucidated owing to their complexity wherein the formation of a particular zeolite can occur by more than one crystallization pathway. Here, we have conducted time-resolved dissolution experiments of MFI-type zeolite crystals in ammonium fluoride medium where detailed structural analysis allowed us to extrapolate and elucidate the possible mechanism of nucleation and crystal growth. A combination of electron and scanning probe microscopy shows that dissolution initiates preferentially at lattice defects and progressively removes defect zones to reveal a mosaic structure of crystalline domains within each zeolite crystal. This mosaic architecture evolves during the growth process, reflecting the changing conditions of zeolite formation that can be retroactively assessed during zeolite crystal dissolution. Moreover, a more general implication of this study is the establishment that dissolution can be used successfully as an ex situ technique to uncover details about crystal growth features inaccessible by other methods.

INTRODUCTION

Zeolites are a family of crystalline microporous tectosilicates that are extensively used as heterogeneous catalysts, molecular sieves, sorbents, and ion exchangers. The large-scale production of synthetic zeolites already has more than a half-century history. At present, the annual production is above 3 million tons/year (*1*). About 10 different types of zeolites are being used on a large industrial scale, and the number of zeolites used in niche markets is larger. These figures demonstrate the maturity of large-scale production of zeolites. Nevertheless, there are certain aspects of zeolite formation mechanism(s) that remain to be clarified.

The difficulty in understanding zeolite crystallization is mainly due to the heterogeneity of the growth mixtures containing solid and liquid components and the presence of a myriad of different species (i.e., precursors) (*2*). The complex interactions between these species and condensation steps leading to the formation of aluminosilicate frameworks around an inorganic and/or organic structure-directing agent are also difficult to be traced and unambiguously determined. Further uncertainty is compounded by the fact that the formation of a particular zeolite could occur by more than one crystallization pathway (*3*–*5*). Different methods providing information about the short- and long-range order in aluminosilicates, their chemical composition, and molecular interactions have been used to shed light on the events preceding zeolite nucleation and the subsequent growth process (*2*–*11*). Thus, zeolite formation has been studied by a variety of scientific approaches to gain a more complete picture of the factors guiding the growth of a particular zeolite. For instance, snapshots of a particular stage of zeolite formation were obtained by in situ analysis using specially designed equipment (*3*, *4*, *12*). Molecular modeling has also been used to decode zeolite formation in combination with experimental analyses (*13*–*15*). These continuous efforts have resulted in a generally accepted mechanism that describes the major stages of crystallization without, however, being able to provide a basis for zeolite synthesis by design (*10*, *16*).

Studies focused on characterizing local zeolite structure have allowed for the identification of nucleation and growth of zeolites. Still, even these studies have not provided molecular-level information on the various pathways involved in zeolite crystal growth (*3*, *4*, *6*, *7*). Understanding the growth history and establishing a detailed picture of each stage of zeolite formation would advance efforts to obtain a product with desired physicochemical properties; however, such a thorough, comprehensive analysis of the growth process for a single crystal is difficult to acquire with the currently available methods.

In this study, we use a nontraditional approach to study crystallization mechanisms: dissolution in an ammonium fluoride medium. Dissolution offers a route to identify defects or irregularities in crystals that form during growth where the chemical bonds that break first would be corresponding to the weak bonds in the crystal. Following the critical aspects of aluminosilicate dissolution, as summarized in detail by Crundwell (*17*–*20*), it is considered that, during dissolution experiments, the domains corresponding to stable, viable nuclei should dissolve last. Hence, the dissolution of the zeolite structure can be used to reveal information about the critical steps during nucleation and growth. Such an approach allows for valuable insights of the growth process to be disclosed by identifying regions with a high density of defects in the crystal and their role in various stages of crystallization, i.e., the temporal trajectory of zeolite formation. The above presumption could be correct only when the etching agent is not chemically selective and will not react preferentially with the chemically inhomogeneous zones in the crystal (i.e., preferential removal or Si or Al in aluminosilicates). This differs from the vast majority of processes reported in literature where dissolution has been used. For instance, etching is largely used for

[1]Central Facility for Advanced Microscopy and Microanalysis, University of California, Riverside, CA 92521, USA. [2]Department of Chemical and Biomolecular Engineering, University of Houston, Houston, TX 77204, USA. [3]State Key Laboratory of Heavy Oil Processing, College of Chemical Engineering, China University of Petroleum (East China), Qingdao 266580, China. [4]Shared Equipment Authority, SIMS Laboratory, Rice University, 6100 Main Street, Houston, TX 77005, USA. [5]Ruđer Bošković Institute, Division of Materials Chemistry, Laboratory for Synthesis of New Materials, Bijenička cesta 54, Zagreb, Croatia. [6]Qingdao Institute of Bioenergy and Bioprocess Technology, Chinese Academy of Sciences, Qingdao, Shandong 266101, China. [7]Normandie Université, ENSICAEN, UNICAEN, CNRS, Laboratoire Catalyse et Spectrochimie, 6 Boulevard Marechal Juin, 14050 Caen, France.
*Corresponding author. Email: valentin.valtchev@ensicaen.fr
†These authors contributed equally to this work.

the postsynthesis modification of zeolite properties (*21*–*23*). Steaming is a commercial method for increasing the Si/Al ratio in zeolites (*24*, *25*). Such a study performed on a single zeolite particle level, using Zeolite Socony Mobil-five material (ZSM-5) as a model material, revealed that the steaming renders its surface rough and generates mesoporosity (*26*). This greatly improved the accessibility, but at the same time, the strength of the Brønsted acid sites decreased. Mineral acids are also used to extract Al from zeolite frameworks, while caustic solutions are used to preferentially remove Si (*27*–*30*); however, these chemically selective etchants cannot be used to study the crystal growth of a zeolite.

Here, we examine the unbiased dissolution of Mordenite Framework Inverted (MFI-type) zeolite crystals in a fluoride medium at both macroscopic and molecular levels. Our recent results have shown that upon dual hydrolysis, the compound NH_4F forms species that dissolve Si and Al at similar rates (*31*). Etching by NH_4F was used to obtain hierarchical materials with retained framework composition (*32*). In the present study, we have used unbiased chemical etching to reveal evidence of the zeolite crystallization mechanism. This process also provides insights into the intimate structure of a crystal on the basis of molecular reversibility since the weak bonds break first, and the stable, coherent domains dissolve last, which allows for the facile detection of defects within the structure. This study is performed on large crystals of ZSM-5 (Si/Al = 91) and its siliceous isostructural form silicalite-1, which allows for clearer visualization of any particularity in the growth process. The use of a siliceous and Al-containing sample was necessary to evaluate the impact of aluminum on the growth and on the dissolution process, respectively. For the sake of comparison, a low-silica ZSM-5 material (Si/Al = 21) synthesized in a basic medium was also included in the study.

RESULTS

From powder x-ray diffraction (XRD) analysis, the sharp peaks in XRD spectra showed that all used MFI samples are highly crystalline (fig. S1A). The N_2 adsorption-desorption isotherm (fig. S1B) is type I, which is characteristic of microporous materials. The micropore volume of MFI-type materials, calculated using the *t*-plot method, is ca. 0.16 cm^3/g, a value typical for highly crystalline MFI-type materials. Scanning electron microscopy (SEM) inspection revealed that the ZSM-5(91) crystals are uniform in size and approximately 100 to 120 μm in length (i.e., the *c* direction; fig. S1C). Silicalite-1 crystals synthesized in fluorine medium are a little bit shorter, ranging between 80 and 100 μm. ZSM-5(21) sample also exhibits well-shaped crystals with a size of about 5 μm. Most of the crystals have a well-defined morphology with the typical coffin shape, and a few agglomerates can be observed.

The surface features of ZSM-5(91) crystals from SEM are shown in Fig. 1A. Different levels of crystal etching, from the as-synthesized sample until later times when the initial crystal morphology is indiscernible, are presented in Fig. 1 (C to F). After 30 min of treatment in NH_4F, only the interface between twinned zeolite crystals is dissolved, as can be seen in Fig. 1B, showing the dissolved interface between two contact twins oriented at 180° relative to each other. Figure 1C shows the dissolution of the interface between an 80-μm-long crystal and surface twins rotated at 90°. After 60 min of treatment, deeper dissolution reveals interior features building the apparent "single" crystals (Fig. 1D); and after 120 min of etching, only fragments of the original crystal remain where cavities with angular

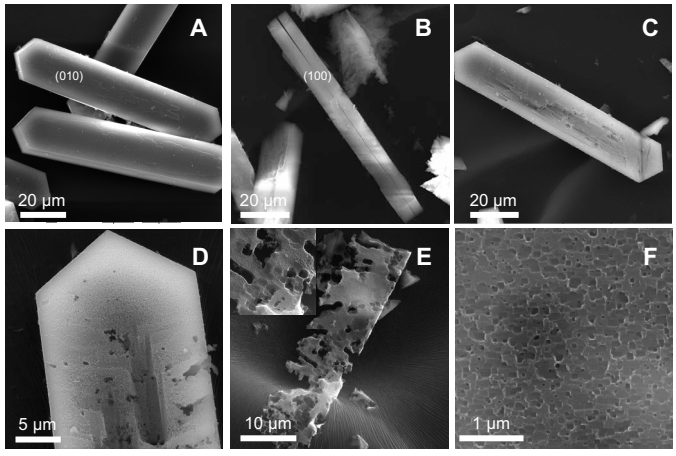

Fig. 1. Scanning electron micrographs of parent ZSM-5(91) and partially dissolved crystals obtained after different periods of etching. (**A**) Parent crystals used for the dissolution experiments; (**B**) morphology and features of reaction products after 30 min of dissolution; (**C**) representative crystal subjected to 60 min of treatment; (**D**) higher-magnification view of the (010) facet of a crystal after 60 min of treatment; (**E**) representative crystal subjected to 120 min of treatment; and (**F**) high-magnification view of the (010) surface of a crystal after 120 min of etching.

outlines can be seen (Fig. 1, E and F). These observations show that the dissolution process is steered by distinct crystallographic zones with a clear hierarchical organization. Namely, at the micron scale, the interfaces between the twin crystals are preferentially dissolved (Fig. 1, B to D), and on a nanometer scale, the dissolution follows particular crystallographic directions since dissolution pits exhibit well-defined straight facets, with a pseudohexagonal shape (Figs. 1 and 3). Furthermore, we observe that the crystal core is more extensively dissolved than the peripheral regions of the crystals. To better understand the phenomenon controlling the dissolution process, complementary imaging methods were used.

Atomic force microscopy (AFM) was used to examine time-resolved changes in surface topography during crystal dissolution. Conducting in situ measurements was challenging due to the debris generated at the interface; therefore, we used an ex situ protocol (fig. S2) wherein the same surface of a zeolite crystal was imaged after various intervals of NH_4F treatment (fig. S3). After each interval of the treatment, a series of AFM images was taken over an entire (010) surface and combined into a composite figure (figs. S3 and S4A), where specific regions could be evaluated to track distinct changes in surface features with time. There were three general types of features observed in AFM images: crevices, etch pits, and spheroidal domains. The generation of crevices (that corresponds to the area marked in fig. s4A; Fig. 2) seems to originate at (100) edges of the crystal and propagate inward with temporal increases in crevice width and depth (Fig. 2D). Multiple ex situ images of the crystal surface are compiled in movie S1 where periodic snapshots during 60 min of treatment (Fig. 2, E to J) reveal notable changes in surface topography. The initially rough surface of the untreated crystal becomes relatively smooth after 10 min of treatment due to the removal of large features present on as-synthesized substrates; and with prolonged treatment, AFM images reveal the emergence of crevices and etch pits. Similar to field-emission SEM images in Fig. 1, we observe heterogeneous surface topographies with prolonged dissolution time.

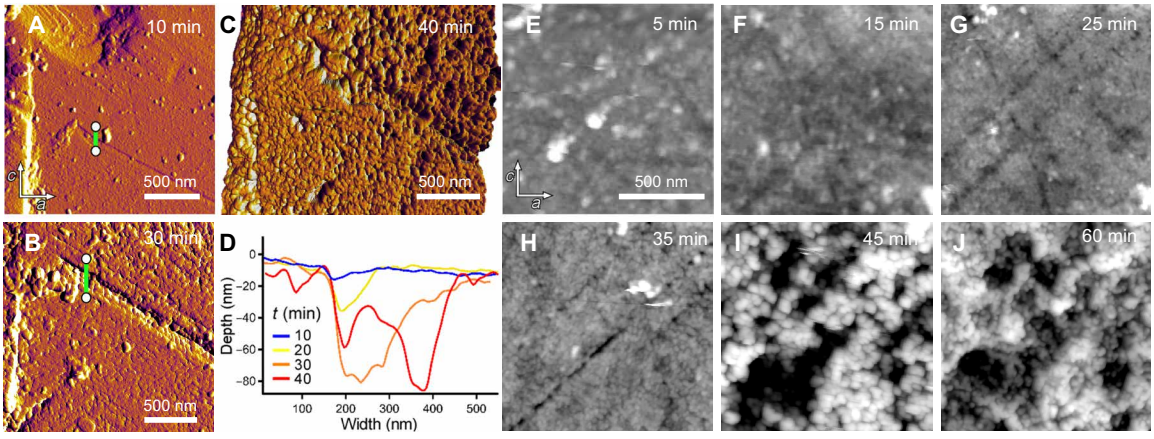

Fig. 2. AFM analysis of silicalite-1 (010) surface dissolution. (**A** and **B**) Time-elapsed images between 10 and 30 min of treatment showing the development of a crevice. (**C**) Three-dimensional rendering of overlapping height and amplitude images showing the crevice after 40 min of treatment. (**D**) Height profiles along the green lines in (A) and (B) showing the increased depth and width of the crevice with treatment time (data are normalized to the baseline). (**E** to **J**) Height images of a different surface between 5 and 60 min of treatment at a fixed imaging area. The full sequence of time-resolved images is compiled in movie S1.

Some regions remain relatively smooth with less evidence of dissolution, whereas other regions develop highly roughened or pitted surfaces (fig. S3). Images after 45 min of treatment (Fig. 2I) show the presence of spheroidal domains and etch pits that become enlarged with further treatment (Fig. 2J). The size distribution of etch pits after 60 min of NH_4F treatment is shown in fig. S3. The AFM analysis demonstrates the inequivalent spatial dissolution of the zeolite crystal surface, which is not related with the framework composition since this series of experiments was performed on silicalite-1 crystals. Thus, surfaces exhibiting disproportionately high rates of dissolution are attributed to zeolite crystal imperfections (i.e., defect zones present on crystal facets).

Later stages of dissolution, when etch pits became too deep for analysis by AFM, were studied using a combination of SEM, transmission electron microscopy (TEM), and scanning TEM (STEM). Representative images of ZSM-5(91) and silicalite-1 crystal dissolution after 30 and 60 min are shown in Fig. 3 (A to C and D to F, respectively). The backscattered electron (BSE) image of ZSM-5(91) (Fig. 3A) and the TEM bright-field image of silicalite-1 (Fig. 3D) both reveal zonal growth patterns. In particular, the hourglass feature (Fig. 3D) suggests sectorial growth starting from the crystal core, consistent with previous studies of large MFI-type crystals and of hollow zeolite structures (*33*, *34*). Electron micrographs showed that the dissolution along the interface between the 90° and contact twins in ZSM-5(91) crystals is due to the presence of highly strained zones between the individual crystals; however, the origin of small etch pits with pseudohexagonal shape formed deep within the core of the crystals is not immediately obvious. It is revealed (Fig. 3, C and F) that the facets outlining the etch pits are parallel to low-index atomic planes, such as (001) and (101), clearly exhibiting crystallographic control of dissolution on the unit cell level.

In a previous study, we suggested that the mosaic of pseudohexagonal etch pits might be due to the dissolution of misoriented crystalline domains. Here, this hypothesis is verified by high-resolution TEM (HRTEM) imaging down the *c* axis of ZSM-5(91) crystal. As shown in Fig. 4, thin electron transparent lamellas were cut perpendicular to the *c* axis by focused ion milling from two different regions

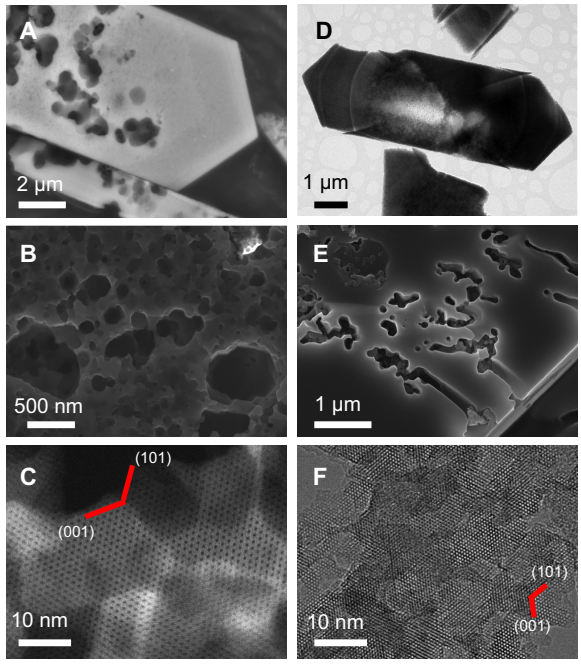

Fig. 3. Dissolution uncovers the history of ZSM-5(91) and silicalite-1 crystallization. (**A**) Zonal growth structure in the later growth stages is revealed by BSE imaging of ZSM-5(91) crystal treated for 30 min. (**B**) SEM image of ZSM-5(91) crystal treated for 60 min highlighting dissolution pits on the {010} face with pseudohexagonal shapes and straight edges parallel to low-index atomic planes, such as {001}, {101}, and {10$\bar{1}$}. (**C**) High-angle annular dark-field HR-STEM image along the ⟨010⟩ axis of the same specimen shown in (B). The dark spots in the structural images correspond to the channels in the structure, and the bright lines are the SiO_4 tetrahedral chains. (**D**) TEM bright-field image of a silicalite-1 crystal treated for 60 min. (**E**) SEM image of the {010} face of a silicalite-1 crystal treated for 30 min revealing the pseudohexagonal shape of dissolution pits that appear more irregular than those of ZSM-5(91). (**F**) Corresponding HRTEM image down the ⟨010⟩ axis from the same specimen in (E). The bright spots here correspond to the open channels of the zeolite structure and the dark areas to the framework. The orientation of the traces of the {001} and {101} planes is marked with red lines in (C) and (F).

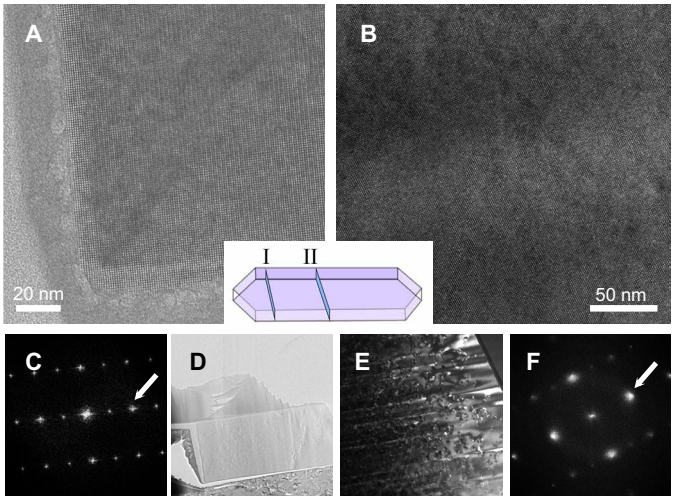

Fig. 4. TEM images of FIB thin sections cut perpendicular to the *c* axis from an as-synthesized ZSM-5(91) crystal not subjected to dissolution treatment. HRTEM images down the *c* axis of foils from the periphery (**A**) and the central part (**B**) of the crystal. (**C** and **F**) FFTs from the lattice images in (A) and (B), respectively, with marked 020 reflections. (**D**) Low-magnification image of one of the FIB foils. (**E**) Low-magnification TEM dark-field image from the foil cut from the central part of the crystal. Inset: Schematic of the sites for cutting sections I (periphery) and II (center) from the as-synthesized crystal.

of the same crystal. The first lamella was cut from the peripheral region of the crystal close to the apical tip (Fig. 4, A, C, and D), labeled as "I" in the inset of Fig. 4. The second was cut from the central part of the crystal (Fig. 4, B, E, and F) and is labeled "II." The crystal structure and order in lamella I appear perfect with no notable defects or distortions (Fig. 4A), also confirmed by the sharp, bright spots in the corresponding fast Fourier transform (FFT) pattern (Fig. 4C). In contrast, closer inspection of HRTEM images of lamella II (Fig. 4B) reveals the existence of a mosaic structure in the center of the crystal that is composed of fine domains slightly misoriented with respect to each other by minor mutual rotation within the plane of imaging. The fine domains are confirmed both by dark-field contrast imaging (Fig. 4E) using 020 reflections and by the shape and size of the 010, 020, and 200 reflections in the FFT pattern (Fig. 4F). The diffuse character of the spots in Fig. 4F can be attributed to misorientation between the fine domains in this region of the crystal. A comparison between the same type of reflections (marked by white arrows in Fig. 4, C and F, respectively) demonstrates the difference in crystalline ordering of the peripheral and central parts of the crystal. The sharp character of the FFT spots in Fig. 4C is a clear evidence of a defect-free structure as opposed to the mosaic domain structure revealed in Fig. 4F.

The above interpretation is further corroborated by cutting a thin focused ion beam (FIB) section perpendicular to the *c* axis from the middle of another ZSM-5(91) crystal (fig. S5). The misorientation between adjacent domains is minor and difficult to discern directly from HRTEM images. Hence, the same digital processing was applied to the images taken in the middle and the periphery of the foil (cut from the central part of untreated ZSM-5 crystal) to enhance the contrast. First, FFT was applied to the HRTEM images to obtain the patterns shown in fig. S5 (C and D), and then a circular filter was applied to select only the reflections up to (200) and (020) in the FFT patterns (insets in fig. S5, C and D). Inverse FFT processing of the aforementioned filters resulted in the images shown in fig. S5 (A and B). The uniform appearance of the filtered inverse FFT image in fig. S5B (i.e., the lack of contrast variation across the lattice fringes), in comparison to the nonuniformity of the image of the central part (fig. S5A), confirms the defect-free nature of the peripheral parts of the ZSM-5(91) crystals. This is consistent with the sharp reflections seen in the FFT pattern from the periphery (fig. S5D) compared to the more diffused appearance of the FFT reflections (fig. S5C) from the HRTEM image of the central region. Fine domains between 10 and 25 nm in diameter are visualized by HRTEM imaging after processing in the central part of the thin foil (fig. S5, A and C), revealing the mosaic structure of the central region of ZSM-5(91) zeolite crystals due to minor misorientation of neighboring domains. Such domains are missing in the periphery of the foil (fig. S5, B and D), indicating that this region has little to no defects.

The difference in the dissolution of the peripheral and central parts of the crystal is also observed by chemical mapping via time-of-flight secondary ion mass spectrometry (TOF-SIMS) of untreated silicalite-1 crystals (fig. S6, A to D) compared to those after 60 min of treatment (fig. S6, E to H). The trace quantity of the organic structure-directing agent [tetrapropylammonium (TPA)] provides a high contrast wherein the tracking of TPA ion fragments ($C_3H_8N^+$) in the crystal before and after treatment (fig. S6, B and F, respectively) reveals distinct regions of dissolution. Similar information with less sensitivity can be gleaned from TOF-SIMS mapping of SiO^+ (fig. S6, C and G) and Si_2OH^+ (fig. S6, D and H) ions, which reveal a difference in Si—O bonds and terminal silanol groups between the peripheral and central regions of the silicalite-1 crystals. In addition, we used ex situ AFM to monitor the evolution of spheroidal domains during NH_4F treatment of a silicalite-1 (010) surface. High-resolution images of a fixed area on the crystal surface (Fig. 5, A to D, and movie S3) reveal the progressive appearance of small spheroidal domains that seemingly dissolve at a much slower rate than the surrounding regions (Fig. 5G). Similar features were observed in multiple regions of several crystals during AFM measurements (e.g., Fig. 2I and movie S1). Analysis of height images for several crystals in a single dissolution experiment reveals a distribution of spheroidal feature sizes (Fig. 5F) with an average diameter of 15 nm. This is consistent with the domain sizes determined by HRTEM imaging (fig. S5) corresponding to interior regions of the crystal, where more defects are observed. The classification of spherical domains as either amorphous or crystalline cannot be gleaned from AFM images; however, we surmise that these features are predominantly crystalline on the basis of several observations. First, the size of spheroidal features is much larger than those of amorphous precursors typically encountered in MFI synthesis, which range from 1 to 6 nm (*35*). Previous in situ AFM measurements (*3*) have shown that the attachment of amorphous precursors to MFI crystal surfaces is followed by a disorder-to-order transition wherein precursors become integrated into the underlying crystal interface. It is possible that a fraction of amorphous-to-crytalline transformations are incomplete, leading to the occlusion of disordered domains as defects within zeolite crystals. We posit that these events are rare and do not account for the large population of 15-nm spheroidal domains observed in AFM images (Figs. 2 and 5). This is consistent with HRTEM images (Figs. 3 and 4) that lack evidence of amorphous domains, which would be expected to extend well beyond that of a single particle to encompass the large areas observed in AFM

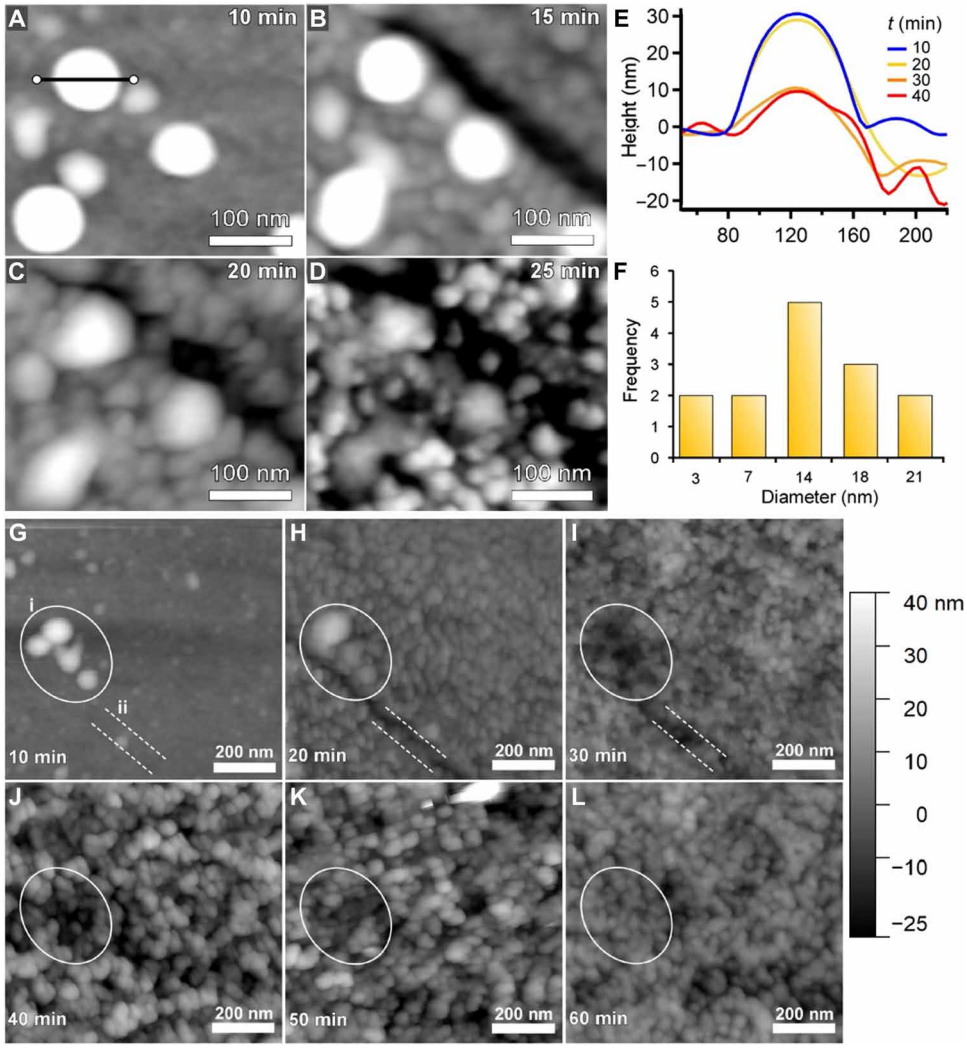

Fig. 5. AFM analysis of the dissolution of silicalite-1. (**A** to **D**) AFM height images of a fixed area on a silicalite-1 (010) surface between 10 and 25 min of treatment. The images were taken from the region highlighted in fig. S4A, and the full compilation of time-resolved images is compiled in movie S2. (**E**) Height profiles of a feature in AFM images (marked with a black line) after the following treatment times: 10 min (blue), 20 min (yellow), 30 min (orange), and 40 min (red). (**F**) Analysis of AFM images over the entire crystal surface after 60 min of treatment reveals a distribution of spheroidal feature diameters ($n = 17$ measurements). The diameters are median values (±2 nm) adjusted to account for the AFM tip curvature (see fig. S2B). (**G** to **L**) AFM height images of a fixed silicalite-1 (010) surface area between 10 and 60 min of treatment. A full compilation of time-resolved images (5-min intervals) is shown in movie S3. The color gradient, which correlates to height (nanometers), is constant for all images. Several features [white oval (i)] during dissolution alternate between smooth to rough topographies as spheroidal features progressively emerge from the dissolving interface. These images also show a crevice [double white dashed lines (ii)] that becomes less prominent with prolonged treatment as the difference in height between the depth of the crevice and the crystal surface decreases. A corresponding set of amplitude images is included in fig. S7. The area selected for analysis is marked in fig. S4A.

images (e.g., Fig. 5J) with high densities of spheroidal features. Hence, these spheroidal features are likely crystalline nanoparticles that incorporate into zeolite crystals via a mechanism of (nearly) oriented attachment.

The crystal growth pattern of MFI-type zeolite is clearly revealed by dissolution experiments. As shown in Fig. 3 and fig. S6, the interior regions of the crystal dissolve much more rapidly than the periphery. Furthermore, TEM imaging clearly reveals an "hourglass" feature in the center of most partially dissolved crystals. This hourglass zone is overgrown by zonal features (Fig. 3, A and D). The above observations are evidence of multistage crystal growth, where the growth mechanism changes from sectorial to zonal growth over the course of crystallization.

The characteristics of late-stage zonal growth are further exhibited by a closer examination of temporal changes in surface topography of facets during the final growth stages. The growth terraces visualized in SEM images (fig. S8) demonstrate, first, that the growth at this stage proceeds by the layer-by-layer zonal growth mechanism. Second, it shows that the growth most probably takes place by agglomeration of viable globular proto-crystals with sizes between 5 and 25 nm in diameter, rather than direct incorporation of dissolved ionic or molecular species from the solution.

AFM imaging (fig. S3) also confirms the presence of nonuniform regions (micron-size areas) where dissolution is more prevalent in some locations, whereas others are less affected by the treatment. Time-resolved analysis of the silicalite-1 (010) surface during

dissolution also reveals dynamic sequences of emerging and disappearing features leading to either a smooth or rough surface topography. For example, AFM height images of a fixed area over a 60-min period of dissolution (Fig. 5, G to L) and corresponding amplitude images (fig. S7) reveal the initial presence of large protrusions (highlighted by the dashed oval) that disappear with treatment time to yield an interface with either flat regions or spheroidal features.

DISCUSSION

The applied approach has allowed us to reveal critical details about the zeolite dissolution process and, in turn, about the intimate structure of the studied MFI-type materials. The following conclusions can be drawn regarding the dissolution process. Dissolution is selective for regions with higher densities of defects, which are nonuniformly distributed throughout the crystal. The etching agent attacks predominantly the central parts of the MFI-type crystals and affects the periphery of crystals to a significantly lesser extent, which corresponds to their relative concentration of defects (Fig. 4 and fig. S4).

Our analyses have shown that the crystals are chemically homogeneous and structurally, on a micron-scale level, well crystallized with some degree of twining. The studied MFI-type samples are essentially built up by SiO_4 tetrahedra, where all oxygen atoms are shared. Hence, there is no significant structural anisotropy in the bond strength across individual tetrahedra, which can affect the dissolution process (*17*–*20*). The main factor that would affect Si—O bond strength is protonation; however, since the crystal is compositionally homogeneous, protonation should not affect the dissolution process selectively. Consequently, the primary cause of dissolution is the presence of defects on atomic and unit cell levels, which can introduce inhomogeneity and selective bonding among the SiO_4 tetrahedral framework. Different types of defects in crystalline materials are presented in fig. S9. Our observations suggest that dissolution starts at defect sites with strained T—O bonding, such as point defects, dislocations, twin boundaries, and low-angle grain boundaries. It proceeds by expanding around initially formed dissolution pits. The dissolution advances parallel to low-index atomic planes with small reticular density, which seemingly follows a reciprocal Bravais-Friedel-Donnay-Harker (BFDH) growth law (*36*) at a localized level. The BFDH growth law stipulates that the morphological importance of crystal faces is reciprocally proportional to the reticular density of the atomic planes, expanded later by Hartman and Perdok (*37*), relating the reticular density to the crystal bond strength between building constituents. The crystal periphery appears to be the most stable, which accounts for our observation that this region dissolves at a much slower rate. In the late stages of zeolite formation, the growth rate is relatively slow and likely accounts for the presence of fewer defects in peripheral crystal zones, thereby leading to higher structural order in these regions (Figs. 3 to 5).

Our previous study of zeolite Linde Typa A (LTA) showed that nucleation occurs within agglomerates of amorphous (alumino)silicate precursors (*6*). The latter species coalesce with synthesis time into larger particles with a crystalline structure and an overall size of a few to tens of nanometers, forming stable nuclei that can interact and fuse with other nuclei throughout the crystallization process. A similar process for MFI-type zeolite was reported (*38*) using cryo-TEM to track various stages of nucleation to confirm growth by a nonclassical multistep mechanism (*39*). Following the above observations as well as those from this study, our interpretation of the nucleation and crystallization process is summarized schematically in Fig. 6. The initial incubation period is marked by the formation of fine crystalline proto-particles (Fig. 6A, step I). During the coalescence of these particles, the formation of domain boundaries (marked by red dashed lines in Fig. 6A, step II) is proposed where the fast fusion between them creates a mismatch between the crystalline

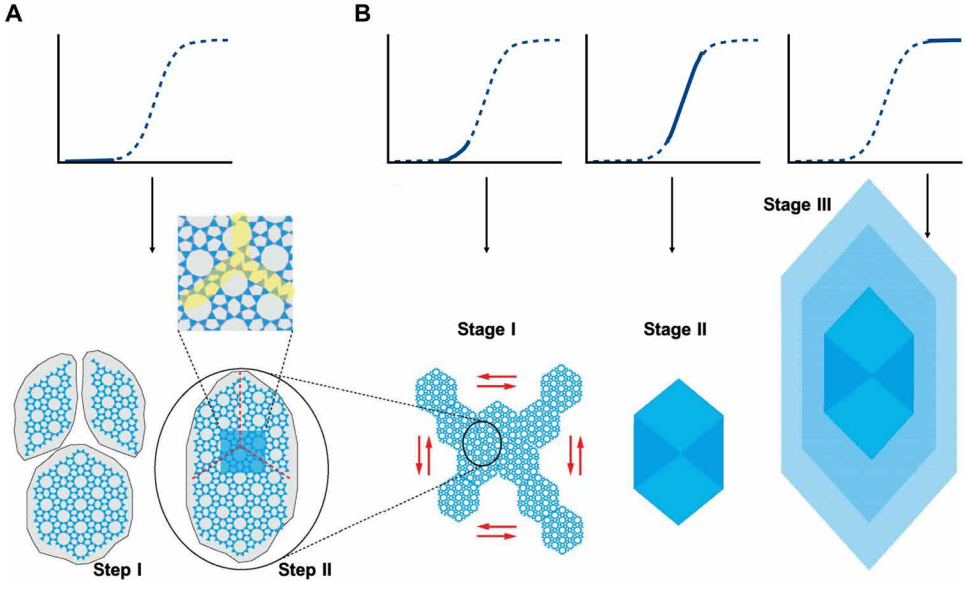

Fig. 6. Schematic drawing of the interpretation of the growth process in the studied MFI system. (**A**) The incubation process involves two steps: (I) formation of proto-particles with MFI structure and (II) fusion of these particles to form nuclei. Structural discrepancy boundaries are marked with broken red lines. The shaded central part of the nucleus corresponds to the enlarged inset, and the structural discrepancy boundaries are marked in yellow. (**B**) The growth process has three distinct stages: (I) skeletal growth, (II) sectorial growth, and (III) final zonal overgrowth. Each phase is correlated with the crystal growth period in the crystallization curve depicted in the top part of the scheme.

structure of each particle. The process is statistical in nature; some of the discrepancies and distortions that have higher interface energy are eliminated by minor rearrangements; others are sealed and preserved as fine-size domains through the subsequent stages of crystal growth. Some of these intergrowing domains give rise to twin relationships and likely serve as a starting point for twin growth; others have mismatch that leads to low-angle domain boundaries, dislocations, and point defects. The vacancies between crystalline domains can be sealed by the addition of low–molecular weight (alumino)silicates (i.e., monomers or oligomers) through crystallization by particle attachment involving the addition of amorphous precursors. The central region of the zeolite crystal forms fast due to a high initial supersaturation (including amorphous precursors and soluble species) and a large number of crystallites present, which tends to concentrate a high level of defects, which is anticipated for crystallization by particle attachment (*39*). Moreover, nonclassical pathways involving the addition of amorphous precursors can also lead to defects if the disorder-to-order transition is either incomplete or results in misoriented crystalline domains.

Many of the observations from the study of MFI dissolution are consistent with the processes of zeolite crystallization outlined above. Preferential dissolution at the center of the crystal agrees with the higher number of defective zones created during the early stages of zeolite formation via the agglomeration of MFI nanocrystallites. Consequently, the central part of the crystal is more vulnerable to etching and dissolves more rapidly. It is apparent that zeolite formation in the studied system is a complex multistage process, as the mechanism of growth is a function of the supersaturation, which differs in the early and late stages. It can be speculated that the initially formed nuclei rapidly assemble into a skeletal structure along the ⟨101⟩ directions (stage I in Fig. 6B), setting up the growth process of the subsequent stage II that proceeds by sectorial growth originating from the skeletal structures formed in stage I (stage II in Figs. 6B and 3D). This is facilitated further by the high concentration of nuclei present in the solution. The final stage is marked by a lower concentration of reactive species and a slower growth rate, leading to peripheral regions with fewer defects that exhibit slower rates of dissolution. The large size of the crystallites formed already predetermines zonal layer-by-layer growth (*40*) following rapid nucleation and growth in the crystal core. The participation of the preformed particles, which we evaluated to be in the range of 5 to 25 nm (Figs. 3, C and F, and 5F and fig. S5A), is limited during the late stage of zeolite growth. Growth and dissolution are competing processes resulting in the final crystal form, which is faceted by low-index slow-growing faces.

The reported results were obtained by studying large zeolite crystals grown in a fluoride medium. The validity of the findings was verified by a study on conventional ZSM-5(21) crystals synthesized in a basic medium. The small crystal size (ca. 5 μm) is not appropriate for an AFM investigation. Thus, the dissolution process was followed by a combined SEM-TEM analysis. Representative SEM and TEM micrographs of the crystals subjected to 20, 40, and 60 min of 40 weight % (wt %) NH_4F solution etching are shown in fig. S10. After 20 min of etching, the twin crystals were separated (fig. S10C). Also, the extremity of the crystals, which is formed during the slower zeolite growth in the later stages, was often separated from the core (fig. S10B). After 40 min of etching, the central part of the crystals, which forms during the period of high supersaturation and abundant nucleation (see Fig. 6A) and thus containing a higher number of defective zones, was deeply etched (fig. S10, D and E). Note that the exceptional etching resistance of the surface layer (fig. S10, D and E) formed during the zonal growth (see Fig. 6, stage III). However, the thickness of this layer, which is a result of the zonal overgrowth, was only about 50 nm, while in the case of fluoride medium–grown crystals, it was several microns (Fig. 3A). Deeply etched ZSM-5(21) crystals exhibit a mosaic of rectangular dissolved domains (fig. S10D). Similar dissolution profiles were observed in the large fluoride medium–synthesized ZSM-5 crystals Fig. 1F. Thus, the comprehensive electron microscopy study revealed that the conventional ZSM-5(21) grown in basic medium exhibits the same dissolution profile as the high-silica ZSM-5(91) and all-silica (silicalite-1) counterparts synthesized in fluoride medium. This is an unambiguous proof of the general dissolution mechanism, which allows recovering the zeolite's growing history, reported in the present study.

This study has shown that studying dissolution reactions can be used successfully as a powerful tool to reveal the processes of nucleation and crystal growth down to the atomic level, which are difficult processes to assess in hydrothermal systems by the presently available in situ methods. Furthermore, the vast majority of available in situ methods are, in principle, either of bulk nature or only capable of providing resolution at a micron or larger scale, which prevents direct assessment of the growth process.

The dissolution of MFI-type crystals revealed defects of different types; however, the dominant form of defects and its corresponding concentration and spatial distribution are highly dependent on the "history" of the growing crystals. The stochastic nature of zeolite nucleation and crystal growth leads to particles containing disparate populations of structural defects. The initial period of rapid nucleation in highly supersaturated media generally increases the probability of high defect density within the interior of zeolite crystals, whereas slower growth rates occurring by classical crystallization at later stages of synthesis (i.e., when the nutrient pool is depleted) lead to fewer defects. Thus, the memory of the growth process is coded in the crystal, and the method used in this study using dissolution enables the recovery of a zeolite's growth history. In addition, more general implication of our observations concerns the mosaic structure in crystals that has been known for a long time (*41*), but no direct correlation of its effect on the growth mechanism of microcrystals has been demonstrated until now.

MATERIALS AND METHODS

Zeolite synthesis

ZSM-5 was synthesized from a gel with molar composition of 0.13 TPABr:1.12 NH_4F:0.015 Al_2O_3:1.0 SiO_2:57.87 H_2O. First, aluminum sulfate octadecahydrate (98 wt %; Sigma-Aldrich) and TPA bromide (98 wt %; Sigma-Aldrich) were dissolved in half of the above molar amount of deionized (DI) water to get a clear solution. After that, tetraethyl orthosilicate (98 wt %; Sigma-Aldrich) was added under stirring. The resultant mixture was hydrolyzed overnight at room temperature to get a clear monophasic solution. Then, the NH_4F was dissolved in the second half of the molar amount of the DI distilled water, and the resultant solution was added slowly into the monophasic solution under mechanical stirring. The resultant gel was vigorously stirred for 1 hour and transferred to a 1000-ml Teflon-lined stainless steel autoclave. The synthesis was conducted at 150°C under static conditions. After 7 days of heating, the autoclave was taken out from the oven and quenched immediately in

cool tap water. The solids were recovered by vacuum filtration and subsequently washed with DI water. The solid cake was then recovered and dried at 100°C overnight. The template was removed by calcination at 550°C for 12 hours with a ramp of 6°C/min. The Si/Al ratio of the ZSM-5 samples is 91, and the samples were denoted ZSM-5(91).

Silicalite-1 was synthesized using the same initial reactants and preparation procedure. The molar composition of the initial system was 0.13 TPABr:0.94 NH_4F:1.0 SiO_2:19.29 H_2O. The synthesis was performed at 170 °C for 10 days. A postsynthesis treatment similar to the one applied to ZSM-5 was applied.

A low-silica ZSM-5 sample synthesized in basic medium was included in the study to evaluate the impact of synthesis medium and the high alumina content on the dissolution process. The sample was provided by Clariant. The Si/Al ratio was 21, and the sample was denoted ZSM-5(21).

Fluoride medium etching

Fluoride medium etching of MFI-type material was carried out in NH_4F (98.0%; Sigma-Aldrich) aqueous solution using the following procedure: 7.5 g of the parent, calcined ZSM-5 zeolite was dispersed in 200 g of 40 wt % NH_4F aqueous solution and was allowed to react at 50°C for 20, 40, and 60 min under mechanical stirring and ultrasonic radiation (USC 600 TH, 45 kHz, VWR). Intermediate samples were taken out after a set period of reaction time. The etched products were thoroughly washed with DI water after the fluoride medium treatment.

Characterization

XRD measurements were performed on an X'pert Pro PANalytical diffractometer using Cu Kα radiation (λ = 1.5418 Å, 45 kV, 40 mA). The samples were studied in the 5° to 50° 2θ range with a scanning step of 0.0167° s^{-1}.

Nitrogen adsorption-desorption experiments were performed with a Micromeritics ASAP 2020 automated gas adsorption analyzer. Before analysis, the samples were outgassed at 100°C for 1 hour and 300°C for 12 hours. The Si and Al contents were determined by inductively coupled plasma optic emission spectroscopy (ICP-OES) on an OES 5100 VDV ICP from Agilent; all samples are digested in aqua regia and hydrofluoric acid before the analysis.

Ex situ scanning probe microscopy

AFM measurements of the MFI samples were performed on an Asylum Research Cypher ES Environmental instrument (Santa Barbara, CA) equipped with a liquid sample cell. The silicalite-1 crystals were dispersed on quickset Loctite Epoxy (Henkel Corporation), which was affixed on a 15-mm specimen disc (Ted Pella Inc.). The epoxy was cured in an oven at 50°C, and after 24 hours, the sample disc was removed, cooled to room temperature, and sonicated in DI water to remove loosely bound crystals. The sample disc was then placed in a closed liquid cell. A drop of DI water was deposited on the sample substrate, which, in contact with the AFM cantilever (Oxford Instrument, noncoated silicon nitride), generates an aqueous interface for scanning zeolite surfaces. Images of selected untreated crystals were first collected. The sample disc was then treated in 40 wt % NH_4F solution (98%, NH_4F salt; Sigma-Aldrich) at room temperature. At 5-min intervals, the sample disc was removed from the NH_4F solution, washed with DI water, and scanned by AFM. Because of possible debris on crystal surfaces after each treatment, the selected crystals were cleaned in contact mode before the cantilever was exchanged with a new one for actual imaging. Between treatment intervals, the sample disc was kept submerged in DI water. As initially tracked crystals became unbound from the epoxy after a sequence of treatments, multiple crystals were tracked during the first 60 min of treatment. Images (2 μm by 2 μm or 3 μm by 3 μm) were collected by moving the cantilever in the *x* and *y* direction on the crystal at set increment. The obtained images were reassembled by overlapping segments to compose an image of a significant portion of the crystal (fig. S2), which allows for ex situ tracking of feature changes as treatment progressed.

Time-of-flight secondary ion mass spectroscopy

Sample preparation

The top mount holder is typically used to handle samples that are very thick (few millimeters) or large (few centimeters). Samples are held in place using double-face carbon. The sample holder was attached to the transfer arm by means of a bayonet fitting, and then the latter is introduced in the load lock chamber until the vacuum pumping reaches a vacuum of 5.0×10^{-5} mbar, ensuring an appropriate detection limit (few parts per million).

Mass spectroscopy

Positive and negative high–mass resolution spectra were performed using a TOF-SIMS NCS instrument, which combines a TOF-SIMS instrument (ION-TOF GmbH, Münster, Germany) and an in situ scanning probe microscope (NanoScan, Switzerland) at the Shared Equipment Authority from Rice University. Bunched 30-keV Bi^{3+} ions (with a measured current of 0.15 pA) were used as a primary probe for analysis (scanned area, 300 μm by 300 μm) with a raster of 128 × 128 pixels. A charge compensation with an electron flood gun has been applied during the analysis. An adjustment of the charge effects has been operated using a surface potential of −120 V and an extraction bias of 0 V for the positive polarity and a surface potential of 90 V and an extraction bias of −20 V for the negative polarity. The cycle time was fixed to 90 μs (corresponding to mass/charge ratio = 0 to 737 atomic mass unit mass range).

Two-dimensional imaging

Bunched 60-keV Bi^{3+} ions (with a measured current of 0.3 pA) were used as a primary probe for analysis (scanned area, 50 μm by 50 μm) with a raster of 2048 × 2048 pixels and then binned to enhance the signal-to-noise ratio. Same conditions of charge compensation have been applied in imaging and in spectroscopy. The number of scans has been limited to five for preventing the damage induced by a high dose of bismuth ions.

The same areas have been analyzed before and after the treatment. Each localized regions of interest have been marked by reference points to provide the highest analysis accuracy in the comparison.

Electron microscopy

Electron beam imaging and analysis were performed at the Central Facility for Advanced Microscopy and Microanalysis at the University of California at Riverside. S/TEM imaging was performed at 80- and 300-kV accelerating voltages in a Thermo Fisher Scientific Titan Themis 300 instrument, fitted with X-FEG electron source, three-lens condenser system, and S-Twin objective lens. HRTEM images were recorded at a resolution of 2048 × 2048 pixels with a Thermo Fisher Scientific CETA-16M complementary metal-oxide semiconductor digital camera with beam convergence semi-angle of about 0.08 mrad. STEM imaging was performed at 300-kV accelerating voltage in the Titan Themis 300 instrument. STEM images

were recorded at a probe convergence of 10 mrad with a probe current of 150 pA, using Fischione Instruments Inc. Model 3000 high-angle annular dark-field detector at a frame size of 2048 × 2048 pixels, dwell time of 15 μs per pixel, and camera length of 245 mm.

TEM sample preparation

For the S/TEM analyses, a small amount of dry reaction powder samples was dispersed in distilled water and ultrasonicated for 5 min to break apart any formed aggregates. A droplet of the resulting suspension was deposited on a TEM grid covered with a thin holey carbon support film.

Thin foils for S/TEM imaging were prepared from individual MFI crystals by cutting thin sections perpendicular to the *c* axis, following established ion milling procedures in a SEM/FIB instrument using Ga ion source (Quanta 200i 3D, Thermo Fisher Scientific). First, a strap of 5-μm-thick protective carbon layer was deposited over a region of interest using the ion beam. Subsequently, an approximately 80-nm-thin lamella was cut and polished at 30 kV and attached to a TEM grid using in situ Oxford Instrument AutoProbe 200 manipulator. To reduce surface amorphization and gallium implantation, final milling at 5 kV and 0.5 nA was used to thin the sample to electron transparency.

Scanning electron microscopy

A Thermo Fisher Scientific Co. Nova NanoSEM 450 was used to study the morphology of the samples. SEM images were acquired using the secondary and BSE mode with a dedicated detector at 2-, 5-, and 15-kV accelerating voltages.

SUPPLEMENTARY MATERIALS

Supplementary material for this article is available at http://advances.sciencemag.org/cgi/content/full/7/25/eabg0454/DC1

REFERENCES AND NOTES

1. Report on global zeolite market; www.grandviewresearch.com/press-release/global-zeolite-market.
2. G. Harvey, L. S. Dent Glaser, Structure and Properties of Aluminosilicate Solutions and Gels, in *Zeolite Synthesis, Symposium Series 398*, M. L. Ocelli, H. E. Robson, Eds. (American Chemical Society, 1989), pp. 49–65.
3. A. I. Lupulescu, J. D. Rimer, In situ imaging of silicalite-1 surface growth reveals the mechanism of crystallization. *Science* **344**, 729–732 (2014).
4. M. Kumar, M. K. Choudhary, J. D. Rimer, Transient modes of zeolite surface growth from 3D gel-like islands to 2D single layers. *Nat. Commun.* **9**, 2129 (2018).
5. F. Schüth, Nucleation and crystallization of solids from solution. *Curr. Opin. Solid State Mater. Sci.* **5**, 389–395 (2001).
6. M. Smaihi, O. Barida, V. Valtchev, Investigation of the crystallization stages of LTA-type zeolite by complementary characterization techniques. *Eur. J. Inorg. Chem.* **2003**, 4370–4377 (2003).
7. E. A. Eilertsen, M. Haouas, A. B. Pinar, N. D. Hould, R. F. Lobo, K. P. Lillerud, F. Taulelle, NMR and SAXS analysis of connectivity of aluminum and silicon atoms in the clear sol precursor of SSZ-13 Zeolite. *Chem. Mater.* **24**, 571–578 (2012).
8. G. Melinte, V. Georgieva, M.-A. Springuel-Huet, A. Nossov, O. Ersen, F. Guenneau, A. Gedeon, A. Palčić, K. N. Bozhilov, C. Pham-Huu, S. Qiu, S. Mintova, V. Valtchev, 3D study of the morphology and dynamics of zeolite nucleation. *Chem. A Eur. J.* **21**, 18316–18327 (2015).
9. S. Mintova, N. H. Olson, V. Valtchev, T. Bein, Mechanism of zeolite A nanocrystal growth from colloids at room temperature. *Science* **283**, 958–960 (1999).
10. R. Aiello, F. Crea, A. Nastro, B. Subotić, F. Testa, Influence of cations on the physicochemical and structural properties of aluminosilicate gel precursors. Part 1. Chemical and thermal properties. *Zeolites* **11**, 767–775 (1991).
11. V. Valtchev, S. Rigolet, K. N. Bozhilov, Gel evolution in a FAU-type zeolite yielding system at 90 °C. *Micropor. Mesopor. Mater.* **101**, 73–82 (2007).
12. L. Ren, C. Li, F. Fan, Q. Guo, D. Liang, Z. Feng, C. Li, S. Li, F.-S. Xiao, UV-Raman and NMR spectroscopic studies on the crystallization of zeolite A and a new synthetic route. *Chem. A Eur. J.* **17**, 6162–6169 (2011).
13. D. P. Petry, M. Haouas, S. C. C. Wong, A. Aerts, C. E. A. Kirschhock, J. A. Martens, S. J. Gaskell, M. W. Anderson, F. Taulelle, Connectivity analysis of the clear sol precursor of silicalite: Are nanoparticles aggregated oligomers or silica particles? *J. Phys. Chem. C* **113**, 20827–20836 (2009).
14. B. Slater, T. Ohsuna, Z. Liu, O. Terasaki, Insights into the crystal growth mechanisms of zeolites from combined experimental imaging and theoretical studies. *Faraday Discuss.* **136**, 125–141 (2007).
15. P. Cubillas, S. M. Stevens, N. Blake, A. Umemura, C. B. Chong, O. Terasaki, M. W. Anderson, AFM and HRSEM invesitigation of zeolite A crystal growth. Part 1: In the absence of organic additives. *J. Phys. Chem. C* **115**, 12567–12574 (2011).
16. W. H. Dokter, H. F. van Garderen, T. P. M. Beleen, R. A. van Santen, V. Bras, Homogeneous versus heterogeneous zeolite nucleation. *Angew. Chem. Int. Ed.* **34**, 73–75 (1995).
17. F. K. Crundwell, The dissolution and leaching of minerals mechanisms, myths and misunderstandings. *Hydrometallurgy* **139**, 132–148 (2013).
18. F. K. Crundwell, The mechanism of dissolution of minerals in acidic and alkaline solutions: Part I--A new theory of non-oxidation dissolution. *Hydrometallurgy* **149**, 252–264 (2014).
19. F. K. Crundwell, The mechanism of dissolution of minerals in acidic and alkaline solutions: Part II application of a new theory to silicates, aluminosilicates and quartz. *Hydrometallurgy* **149**, 265–275 (2014).
20. F. K. Crundwell, On the mechanism of the dissolution of quartz and silica in aqueous solutions. *ACS Omega* **2**, 1116–1127 (2017).
21. M. Milina, S. Mitchell, P. Crivelli, D. Cooke, J. Pérez-Ramírez, Mesopore quality determines the lifetime of hierarchically structured zeolite catalysts. *Nat. Commun.* **5**, 3922 (2014).
22. Z. Qin, J.-P. Gilson, V. Valtchev, Mesoporous zeolites by fluoride etching. *Curr. Opin. Chem. Eng.* **8**, 1–6 (2015).
23. N. Linares, F. G. Cirujano, D. E. De Vos, J. García-Martínez, Surfactant-templated zeolites for the production of active pharmaceutical intermediates. *Chem. Commun.* **55**, 12869–12872 (2019).
24. S. van Donk, A. H. Janssen, J. H. Bitter, K. P. de Jong, Generation characterization, and impact of mesopores in zeolite catalysts. *Cat. Rev. Sci. Eng.* **45**, 297–319 (2003).
25. S. M. T. Almutairi, B. Mezari, E. A. Pidko, P. C. M. M. Magusin, E. J. M. Hensen, Influence of steaming on the acidity and the methanol conversion reaction of HZSM-5 Zeolite. *J. Catal.* **307**, 194–203 (2013).
26. L. R. Aramburo, L. Karwacki, P. Cubillas, S. Asahina, D. A. M. de Winter, M. R. Drury, I. L. C. Buurmans, E. Stavitski, D. Mores, M. Daturi, P. Bazin, P. Dumas, F. Thibault-Starzyk, J. A. Post, M. W. Anderson, O. Terasaki, B. M. Weckhuysen, The porosity, acidity, and reactivity of dealuminated zeolite ZSM-5 at the single particle level: The influence of the zeolite architecture. *Chem. A Eur. J.* **17**, 13773–13781 (2011).
27. R. M. Barrer, M. B. Makki, Molecular sieve sorbents from clinoptilolite. *Can. J. Chem.* **42**, 1481–1487 (1964).
28. M. Tromp, J. A. van Bokhoven, M. T. Garriga Oostenbrink, J. H. Bitter, K. P. de Jong, D. C. Koningsberger, Influence of the generation of mesopores on the hydroisomerization activity and selectivity of *n*-hexane over Pt/mordenite. *J. Catal.* **190**, 209–214 (2000).
29. M. Ogura, S.-y. Shinomiya, J. Tateno, Y. Nara, M. Nomura, E. Kikuchi, M. Matsukata, Alkali-treatment technique—New method for modification of structural and acid-catalytic properties of ZSM-5 zeolites. *Appl. Catal. Gen.* **219**, 33–43 (2001).
30. M. K. Wardani, G. T. M. Kadja, A. T. N. Fajar, Subagjo, I. G. B. N. Makertihartha, M. L. Gunawan, V. Suendo, R. R. Mukti, Highly crystalline mesoporous SSZ-13 zeolite obtained *via* controlled post-synthetic treatment. *RSC Adv.* **9**, 77–86 (2019).
31. Z. Qin, G. Melinte, J.-P. Gilson, M. Jaber, K. Bozhilov, P. Boullay, S. Mintova, O. Ersen, V. Valtchev, The mosaic structure of zeolite crystals. *Angew. Chem. Int. Ed.* **55**, 15049–15052 (2016).
32. Z. Qin, L. Pinard, M. A. Benghalem, T. J. Daou, G. Melinte, O. Ersen, S. Asahina, J.-P. Gilson, V. Valtchev, Preparation of single-crystal "House-of-Cards"-like ZSM-5 and their performance in ethanol-to-hydrocarbon conversion. *Chem. Mater.* **31**, 4639–4648 (2019).
33. L. Karwacki, M. H. F. Kox, D. A. M. de Winter, M. R. Drury, J. D. Meeldijk, E. Stavitski, W. Schmidt, M. Mertens, P. Cubillas, N. John, A. Chan, N. Kahn, S. R. Bare, M. Anderson, J. Kornatowski, B. M. Weckhuysen, Morphology-dependent zeolite intergrowth structures leading to distinct internal and outer-surface molecular diffusion barriers. *Nat. Mater.* **8**, 959–965 (2009).
34. C. Pagis, A. R. Morgado Prates, D. Farrusseng, N. Bats, A. Tuel, Hollow zeolite structures: An overview of synthesis methods. *Chem. Mater.* **28**, 5205–5223 (2016).
35. S. Kumar, T. M. Davis, H. Ramanan, R. Lee Penn, M. Tsapatsis, Aggregative growth of silicalite-1. *J. Phys. Chem. B* **111**, 3398–3403 (2007).
36. J. D. H. Donnay, D. Harker, A new law of crystal morphology extending the Law of Bravais. *Am. Mineral.* **22**, 446–467 (1937).
37. P. Hartman, W. G. Perdok, On the relations between structure and morphology of crystals. I. *Acta Crystallogr.* **8**, 49–52 (1955).
38. T. M. Davis, T. O. Drews, H. Ramanan, C. He, J. Dong, H. Schnablegger, M. A. Katsoulakis, E. Kokkoli, A. V. McCormick, R. L. Penn, M. Tsapatsis, Mechanistic principles of nanoparticle evolution to zeolite crystals. *Nat. Mater.* **5**, 400–408 (2006).
39. J. J. De Yoreo, P. U. P. A. Gilbert, N. A. J. M. Sommerdijk, R. L. Penn, S. Whitelam, D. Joester, H. Zhang, J. D. Rimer, A. Navrotsky, J. F. Banfield, A. F. Wallace, F. M. Michel, F. C. Meldrum,

H. Cölfen, P. M. Dove, Crystallization by particle attachment in synthetic, biogenic, and geologic environments. *Science* **349**, aaa6760 (2015).
40. J. R. Agger, N. Hanif, C. S. Cundy, A. P. Wade, S. Dennison, R. A. Rawlinson, M. W. Anderson, Silicalite crystal growth investigated by atomic force microscopy. *J. Am. Chem. Soc.* **125**, 830–839 (2003).
41. C. G. Darwin, XCII. *The reflexion of X-rays from imperfect crystals*. *London Edinburgh Philos. Mag. J. Sci. London, Edinburgh Dublin Philos. Mag. J. Sci.* **43**, 800–829 (1922).

Acknowledgments
Funding: V.V. acknowledges the financial support from the Industrial Chair ANR-TOTAL "NanoClean Energy" (ANR-17-CHIN-0005-01) and FEDER 18P01675. K.N.B. acknowledges the support for the analytical work by the Office of the Vice-Chancellor of Research and Economic Development at the University of California at Riverside. J.D.R. received support primarily from the U.S. Department of Energy, Office of Science, Office of Basic Energy Sciences under Award Number DE-SC0014468 and additional support provided by the Welch Foundation (Award E-1794). TOF-SIMS analysis was carried out with support provided by the NSF under Award CBET-1626418. This work was conducted in part using resources of the Shared Equipment Authority at Rice University. **Author contributions:** Z.Q. and A.P. prepared the zeolite crystals and performed the dissolution experiments and the general characterization of the samples. K.N.B. performed the electron microscopy study; T.T.L. performed the AFM study; T.T. performed the TOF-SIMS study. V.V. led the overall design and direction of the project. K.N.B., J.D.R., and V.V. prepared the manuscript with help from all authors. **Competing interests:** The authors declare that they have no competing interests. **Data and materials availability:** All data needed to evaluate the conclusions in the paper are present in the paper and/or the Supplementary Materials. Additional data related to this paper may be requested from the authors.

Submitted 8 December 2020
Accepted 30 April 2021
Published 16 June 2021
10.1126/sciadv.abg0454

Citation: K. N. Bozhilov, T. T. Le, Z. Qin, T. Terlier, A. Palčić, J. D. Rimer, V. Valtchev, Time-resolved dissolution elucidates the mechanism of zeolite MFI crystallization. *Sci. Adv.* **7**, eabg0454 (2021).

Science Advances

Time-resolved dissolution elucidates the mechanism of zeolite MFI crystallization

Krassimir N. Bozhilov, Thuy Thanh Le, Zhengxing Qin, Tanguy Terlier, Ana Palcic, Jeffrey D. Rimer and Valentin Valtchev

Sci Adv **7** (25), eabg0454.
DOI: 10.1126/sciadv.abg0454